

Magnetic scattering and electron pair breaking by rare-earth-ion substitution in BaFe₂As₂ epitaxial films

Takayoshi Katase^{1,4}, Hidenori Hiramatsu^{2,3}, Toshio Kamiya^{2,3} and Hideo Hosono^{1,2,3,5}

¹ Frontier Research Center, Tokyo Institute of Technology, S2-6F East, 4259 Nagatsuta-cho, Midori-ku,
Yokohama 226-8503, Japan

² Materials and Structures Laboratory, Tokyo Institute of Technology, 4259 Nagatsuta-cho, Midori-ku,
Yokohama 226-8503, Japan

³ Materials Research Center for Element Strategy, Tokyo Institute of Technology, 4259 Nagatsuta-cho,
Midori-ku, Yokohama 226-8503, Japan

⁴ Present address: Research Institute for Electronic Science, Hokkaido University, Sapporo 001-0020,
Japan

⁵ Corresponding author. E-mail: hosono@msl.titech.ac.jp

PACS numbers: 74.70.Xa, 74.62.-c, 74.25.-q, 72.15.Qm

Abstract.

The effect of electron doping by trivalent charge state rare-earth ion ($RE = \text{La, Ce, Pr, and Nd}$) substitutions on the superconductivity in BaFe_2As_2 was examined using epitaxial films. Each of the RE substitutions suppressed the resistivity anomaly associated with the magnetic/structural phase transitions, leading to the resistivity drops and superconductivity transitions. Bulk superconductivity was observed at the maximum onset critical temperature (T_c^{onset}) of 22.4 K for La-doping and 13.4 K for Ce-doping, while only broad resistivity drops were observed at 6.2 K for Pr-doping and 5.8 K for Nd-doping but neither zero resistivity nor distinct Meissner effect were observed at least down to 2 K. The decrease in T_c^{onset} with increasing the number of RE $4f$ electrons cannot be explained in terms of the crystalline qualities or crystallographic structure parameters of the BaFe_2As_2 films. It was clarified, based on resistivity-temperature analyses, that magnetic scattering became increasingly significant in the above order of the RE dopants. The negative magnetoresistance was enhanced by the Ce- and Pr-doping, implying that the decrease in T_c originates from magnetic pair breaking by interaction of the localized $4f$ orbitals in the RE dopants with the itinerant Fe $3d$ orbitals.

1. Introduction

In the few months since the report on high critical temperature (T_c) superconductivity at 26 K in the 1111-type iron pnictide $\text{LaFeAs}(\text{O}_{1-x}\text{F}_x)$ [1], 122-type AEFe_2As_2 (where AE = alkaline earth) [2] has also joined the family of iron-based high- T_c superconductors as a parent material. To induce its high- T_c superconductivity, both types of doping carrier, i.e. holes and electrons, are typically used by selection of appropriate aliovalent dopants. To date, most such carrier doping processes have been performed by substituting the AE sites with alkali metals with different ion charges, such as K (e.g., in hole-doped $(\text{Ba}_{1-x}\text{K}_x)\text{Fe}_2\text{As}_2$) [2], and by substituting the Fe sites with transition metals with excess 3d electron numbers, such as Co (e.g., in electron-doped $\text{Ba}(\text{Fe}_{1-x}\text{Co}_x)_2\text{As}_2$) [3]. The doping sites are categorized into two modes for 122-type AEFe_2As_2 , i.e., “indirect doping” for doping at sites other than the Fe sites, and “direct doping” for doping at the Fe sites, because the AE and the FeAs layers are spatially separated and the Fermi level is composed mainly of Fe 3d orbitals [4].

The maximum T_c value for each parent material of the iron-based superconductors was obtained by indirect doping [2],[5–7] because direct doping has a major influence on carrier transport in the conducting Fe layer. It was therefore expected that a new indirect electron doping mode for AEFe_2As_2 , e.g. at the AE sites, would lead to high- T_c superconductors, similar to the effects of other indirect doping methods, such as K doping at AE sites (maximum $T_c = 38$ K) [2] and isovalent P doping at As sites (maximum $T_c = 31$ K) [8]. However, indirect electron doping of AEFe_2As_2 by substituting the AE sites with trivalent rare earth (RE) ions was difficult to perform by conventional solid-state reactions; only Ba [9] and Sr [10] have been reported. This difficulty was attributed to electronic instability arising from the high localized density

of states at the Fermi level, as predicted for La-doped $AE\text{Fe}_2\text{As}_2$ [$(AE_{1-x}\text{La}_x)\text{Fe}_2\text{As}_2$] by density functional theory calculations [11,12].

Under such circumstances, indirect RE doping of $AE\text{Fe}_2\text{As}_2$ was achieved by applying a high-pressure synthesis process for $(\text{Sr}_{1-x}\text{La}_x)\text{Fe}_2\text{As}_2$ polycrystals [10] and a melt-growth process using a flux agent for $(\text{Ca}_{1-x}\text{RE}_x)\text{Fe}_2\text{As}_2$ (where $RE = \text{La} - \text{Nd}$) single crystals [13–16]. Among these materials, it should be noted that a Pr-doped CaFe_2As_2 single crystal demonstrated a maximum T_c of 49 K [14], which is the highest reported T_c among the 122-type $AE\text{Fe}_2\text{As}_2$ series, although their shielding volume fractions are as low as $<1\%$ at 40 K [13].

In contrast to the $AE = \text{Ca}$ and Sr systems, there had been no reports on RE -doped BaFe_2As_2 , probably because of the large difference between the ion radii of Ba^{2+} (142 pm for 8-fold coordination) and RE^{3+} (111–116 pm) [17]. However, we recently succeeded in indirect La doping at the Ba sites in BaFe_2As_2 by using a film-growth process [18]. This success was attained by using the highly non-equilibrium nature of thin film deposition via the vapor phase. The maximum T_c (22.4 K) of the $(\text{Ba}_{1-x}\text{La}_x)\text{Fe}_2\text{As}_2$ films was much lower than that of the RE -doped CaFe_2As_2 single crystal, and its electronic phase diagram was almost the same as that of directly-doped $\text{Ba}(\text{Fe}_{1-x}\text{Co}_x)_2\text{As}_2$. On the other hand, according to the scenario in $(\text{Ca}_{1-x}\text{RE}_x)\text{Fe}_2\text{As}_2$ crystals where a smaller RE dopant than La, such as Pr, leads to a higher T_c , we expected that substitution of smaller RE ions with open-shell 4f electrons for the Ba sites would provide a higher T_c than that attained for $(\text{Ba}_{1-x}\text{La}_x)\text{Fe}_2\text{As}_2$.

In this paper, we examined the indirect electron doping of open 4f shell RE ions (Ce, Pr, Nd, and Sm) at the Ba sites in BaFe_2As_2 epitaxial films by pulsed laser deposition (PLD). It was confirmed that three open 4f shell RE dopants (Ce, Pr, and Nd)

were successfully substituted at the Ba sites by the PLD process, similar to the case for La doping. The Ce doping induced bulk superconductivity at a maximum onset T_c (T_c^{onset}) of 13.4 K. On the other hand, although zero resistivity and distinct Meissner effect were not observed down to 2 K, resistivity drops caused by superconducting transitions were observed at 6.2 K for the Pr doping and 5.8 K for the Nd doping. The relationship between the $4f$ electron configuration and the superconducting properties is discussed and comparison is made with the results of the non-magnetic La doping case.

2. Experimental

($\text{Ba}_{1-x}\text{RE}_x$) Fe_2As_2 thin films were grown directly on MgO (001) single crystals with a PLD system using a second harmonic of a Nd:YAG laser as the excitation source [19]. Bulk polycrystalline samples of RE (La, Ce, Pr, Nd, and Sm)-containing BaFe_2As_2 were used as PLD targets (see supplementary Fig. S1 for the synthesis of the bulk polycrystals). Powder X-ray diffraction (XRD, using $\text{CuK}\alpha$ anode radiation) analyses confirmed that the crystalline phases of the bulk polycrystals were mixtures of BaFe_2As_2 and REAs impurity phases, i.e. the RE ions were not incorporated in the BaFe_2As_2 phases [18]. Film growth was carried out at the previously-optimized substrate temperature (T_s) of 850°C (note that the REAs impurity phases appeared in the films at higher values of $T_s > 850^\circ\text{C}$) [18–20]. Each film was 150–250 nm thick, as measured with a stylus profiler. The net doping concentrations in the ($\text{Ba}_{1-x}\text{RE}_x$) Fe_2As_2 films (x_{film}) were measured using an electron-probe microanalyzer (EPMA). The high homogeneity of the RE distribution was confirmed by the EPMA for all of the fabricated samples (see supplementary Fig. S2(a) for mapping images of the RE concentrations). It was also confirmed that x_{film} was controlled by changes in the

nominal *RE* concentration (nominal x) of the *RE*-containing BaFe_2As_2 PLD targets (see supplementary Fig. S2(b) for the relationship between nominal x and x_{film}). The film structures and their crystalline qualities were characterized by high-resolution XRD using $\text{Cu K}\alpha_1$ anode radiation at room temperature. The temperature dependence of the electrical resistivity (ρ - T) was measured by the four-probe method in a temperature range of 2–300 K with a physical property measurement system. Temperature dependence of the magnetic susceptibility (χ - T) was measured with a vibrating sample magnetometer after zero-field cooling (ZFC) and during field cooling (FC).

3. Results

A. Growth of $(\text{Ba}_{1-x}\text{RE}_x)\text{Fe}_2\text{As}_2$ thin films

Figure 1 shows the out-of-plane XRD patterns for films of (a) $(\text{Ba}_{1-x}\text{Ce}_x)\text{Fe}_2\text{As}_2$, (b) $(\text{Ba}_{1-x}\text{Pr}_x)\text{Fe}_2\text{As}_2$, (c) $(\text{Ba}_{1-x}\text{Nd}_x)\text{Fe}_2\text{As}_2$, and (d) Sm-containing BaFe_2As_2 with various values of x_{film} . In the cases of (a) Ce, (b) Pr, and (c) Nd doping, the $(\text{Ba}_{1-x}\text{RE}_x)\text{Fe}_2\text{As}_2$ films obtained were grown epitaxially on MgO substrates with the epitaxial relationship of $[001] (\text{Ba}_{1-x}\text{RE}_x)\text{Fe}_2\text{As}_2 \parallel [001] \text{MgO}$ for the out-of-plane case and $[100] (\text{Ba}_{1-x}\text{RE}_x)\text{Fe}_2\text{As}_2 \parallel [100] \text{MgO}$ for the in-plane case, which is same as that of $(\text{Ba}_{1-x}\text{La}_x)\text{Fe}_2\text{As}_2$ films [18]. The $00l$ diffraction angles of the undoped BaFe_2As_2 film are indicated by the dotted lines to clearly show the peak shift caused by the *RE* substitutions. Sharp $00l$ diffractions of the $(\text{Ba}_{1-x}\text{RE}_x)\text{Fe}_2\text{As}_2$ phases, along with those from a small amount of the Fe impurity phase (indicated by the asterisks), were observed. The $00l$ diffraction peaks shifted systematically to higher angles from the diffraction peaks of the undoped BaFe_2As_2 film as x_{film} increased. The intensities of the Fe impurity diffractions were almost the same in all the samples. Segregation of the

impurity phases of *REAs* started to be observed at the high x_{film} values of 0.30, 0.28, and 0.20 for the Ce-, Pr-, and Nd-doped films, respectively, from which we determined the solubility limits to be lower than these values. Because the formation enthalpies of the *REAs* impurity phases are almost the same (-288 kJ/mol for CeAs, -307 kJ/mol for PrAs, and -304 kJ/mol for NdAs) [22], the different solubility limits are attributed to the differences in the ion size mismatch between Ba^{2+} and RE^{3+} in each case, and in the consequent instability among the $(\text{Ba}_{1-x}\text{RE}_x)\text{Fe}_2\text{As}_2$ phases. In contrast, in the case of Sm doping with $x_{\text{film}} = 0.1$ and 0.17 , no peak-shift of the $00l$ diffractions was detected, and only the segregation of SmAs impurities was observed (Fig. 1(d)), indicating that the incorporation of the smaller Sm ions into BaFe_2As_2 was unsuccessful.

B. Structural characterization

Figure 2(a) summarizes the evolution of the lattice parameters a and c and the unit cell volume V at room temperature as a function of x_{film} for $(\text{Ba}_{1-x}\text{RE}_x)\text{Fe}_2\text{As}_2$ ($\text{RE} = \text{Ce}, \text{Pr}, \text{and Nd}$) epitaxial films. Note that those of the films having the segregated *REAs* phases in Fig. 1 are not plotted because the x_{film} exceeds the solubility limits and the lattice parameters remained almost unchanged from those of the highest x_{film} films in Fig. 2. The c -axis and a -axis lattice parameters were determined by out-of-plane and in-plane XRD, respectively. In all of the dopant cases, systematic shrinkages of the c -axis length were observed (the largest $\Delta c/c$ was $\sim -2.3\%$ for $(\text{Ba}_{1-x}\text{Ce}_x)\text{Fe}_2\text{As}_2$ films with $x_{\text{film}} = 0.28$), while the shrinkage of the a -axis length was very small (the largest $\Delta a/a$ was $\sim -0.3\%$). Consequently, V decreases monotonically as x_{film} increases. These results, which are similar to those obtained for $(\text{Ba}_{1-x}\text{La}_x)\text{Fe}_2\text{As}_2$ [18], substantiate the fact that the RE^{3+} ions substitute the Ba^{2+} sites in the epitaxial films. It is noteworthy

that the c -axis shrinkage increases in the order of Nd, Pr, and Ce dopants, when compared with the same x_{film} , but this result is inconsistent with the differences in the ion radii of the RE^{3+} ions (their radii decrease in the order of Ce^{3+} (114 pm), Pr^{3+} (113 pm), and Nd^{3+} (111 pm) because of the lanthanide contraction) [17]. Additionally, the variation in the a -axis length was independent of the ion radii.

Figure 2(b) shows the x_{film} dependence of the crystalline quality of the $(Ba_{1-x}RE_x)Fe_2As_2$ epitaxial films. Here, the full width at half maximum (FWHM) values of rocking curves for 004 ($\Delta\omega$, out-of-plane) and 200 ($\Delta\phi$, in plane) diffractions were used to evaluate the crystalline quality. The $\Delta\omega$ and $\Delta\phi$ values scatter to an extent but remained almost unchanged at ~ 1.0 degree, regardless of x_{film} for all dopants. Figure 2(c) shows the x_{film} dependence of the FWHM values of 004 diffractions ($\Delta 2\theta$). $\Delta 2\theta$ gradually increased as x_{film} increased, which may originate from the structural strains and/or distortions in the films, probably because of large ion-size mismatches between the Ba^{2+} ion and the doped RE^{3+} ions. However, it is safely concluded that the structural quality is similar for all RE dopants.

C. Transport and magnetic properties

Figure 3 summarizes the ρ - T curves for the epitaxial films of (a) $(Ba_{1-x}Ce_x)Fe_2As_2$, (b) $(Ba_{1-x}Pr_x)Fe_2As_2$, and (c) $(Ba_{1-x}Nd_x)Fe_2As_2$ for various values of x_{film} . The inset figures are magnified views which show the resistivity drops more clearly. The ρ - T curve of an undoped $BaFe_2As_2$ epitaxial film is shown in the top panel of Fig. 3(a) for comparison. The ρ of an undoped $BaFe_2As_2$ film decreases with decreasing T from 300 K, and falls rapidly from ~ 150 K, whose resistivity anomaly is associated with magnetic/structural transitions [23]. As seen in supplementary Fig. S3, a $d\rho/dT - T$

curve provides a clear peak and resistivity anomaly temperatures (T_{anom}). It should be noted that the anomalous temperature range around T_{anom} for the undoped BaFe_2As_2 epitaxial film is broader than that of a single crystal [24]. However, the crystalline quality of this film ($\Delta\omega$ of the 002 diffraction ~ 1 deg.) is almost the same as that of the single crystal ($\Delta\omega$ of the 002 diffraction = 0.7 deg.) [24]. Further, it is reported that a sharp $d\rho/dT$ curve similar to that of the single crystal is observed even in a polycrystal [25]. These results indicate that the broader magneto-structural transition of this film does not originate from a crystalline quality issue. It is reported that a small in-plane stress applied to the BaFe_2As_2 single crystal broadens the structural transition due to the de-twinning of the crystals [26]; therefore, we speculate that a lattice-strain effect at the epitaxial film – substrate interface would be an origin of the broadening. In all dopant cases, ρ at 300 K gradually decreased, and T_{anom} shifted to lower temperatures as x_{film} increased.

In the Ce-doping case (a), a resistivity drop without zero resistivity was observed for $x_{\text{film}} = 0.09$, but the resistivity anomaly was still observed at $T_{\text{anom}} = 70$ K. With a further increase in x_{film} , the resistivity anomaly was not detected in the ρ – T curves, and $T_{\text{c}}^{\text{onset}}$ for a superconductivity transition appears at $x_{\text{film}} \geq 0.09$. $T_{\text{c}}^{\text{onset}}$ reached a maximum value of 13.4 K at $x_{\text{film}} = 0.15$. The resistivity transition width (defined by $\Delta T_{\text{c}} = T_{\text{c}}^{\text{onset}} - T_{\text{c}}^{\text{offset}}$, where $T_{\text{c}}^{\text{offset}}$ is the offset critical temperature determined by extrapolating a ρ – T curve to zero resistivity) of this film is 4.5 K, which is doubly larger than $\Delta T_{\text{c}} = 2.7$ K of La-doped films [18] although the crystalline qualities are almost the same as seen in $\Delta\phi$, $\Delta\omega$ and $\Delta 2\theta$ in Figs. 2(b,c), and the dopant distribution is homogeneous, which is confirmed both by EPMA (see supplementary Fig. S2(a)) and XRD (peak shift and broadening are not observed by Ce doping). Thus, the broad

resistivity transition reflects a wide vortex-liquid-phase due to strong vortex pinning centers, similar to that of the Co-doped BaFe_2As_2 epitaxial film [27,28]. The wide liquid phase is due to disorders in the films, which may also be the case in the Ce-doped films. T_c^{onset} then decreased as x_{film} increased further, and the resistivity drop finally disappeared at $x_{\text{film}} = 0.29$. Also, in the case of Pr doping (b), T_{anom} shifted to lower T values as x_{film} increased and the resistivity drop was observed at $x_{\text{film}} = 0.11$. However, although T_{anom} disappeared at $x_{\text{film}} = 0.18$, clear zero resistivity was not observed at least down to 2 K. On the other hand, in the Nd doping case (c), the resistivity drop was observed at $x_{\text{film}} = 0.13$, but larger values of x_{film} , where the resistivity anomaly is completely suppressed, could not be obtained because of the low solubility limit of the Nd dopant. The maximum transition temperatures of the resistivity drop are 6.2 K and 5.8 K for Pr- and Nd-doping, respectively, but each film did not get into clear superconducting state.

To confirm that the observed resistivity drops originate from superconducting transitions, we measured the magnetic field dependence of the ρ - T curves and the temperature dependence of the magnetic susceptibilities (χ - T) for epitaxial films of $(\text{Ba}_{0.85}\text{Ce}_{0.15})\text{Fe}_2\text{As}_2$ (a), $(\text{Ba}_{0.82}\text{Pr}_{0.18})\text{Fe}_2\text{As}_2$ (b), and $(\text{Ba}_{0.87}\text{Nd}_{0.13})\text{Fe}_2\text{As}_2$ (c), whose chemical compositions were chosen to have the maximum T_c^{onset} for each dopant (Fig. 4). For both measurements, the external magnetic field was applied parallel to the c -axis of the epitaxial films. For all dopants, shifts of T_c to lower T were observed under application of magnetic fields. This result strongly suggests that all the low-temperature resistivity drops originate from superconducting transitions. A clear diamagnetic signal with a shielding volume fraction (SVF) of up to 10% at < 4 K was observed only in the case of Ce doping. Note that, the Meissner effect starts to appear at a temperature of

$T_c^{\text{Meissner}} \sim 7.8$ K, which is almost the same as $T_c^{\text{zero}} \sim 8.0$ K where the resistivity reaches zero. However, the SVFs of the superconducting phases in the Pr- and Nd-doped films are very low because no Meissner effect is observed in their χ - T curves. This observation suggests a possibility that the observed resistivity drops in the Pr- and Nd-doped films come from a superconducting transition from impurity phases; however, the impurity phase detected by XRD (Fig. 1) was only Fe, which does not show superconductivity at $T \geq 2$ K. It is hard to consider that an amorphous impurity caused the superconductivity-like resistivity drops; therefore, we consider that the Meissner effect was not observed for the Pr- or Nd-doped film because T_c^{Meissner} would be lower than the temperature range examined in this study (i.e., < 2 K). As a consequence, we conclude that the resistivity drops are caused by superconducting transitions of the Pr- and Nd-doped BaFe_2As_2 phases. Considering that perfect diamagnetism with an SVF of 100% at $T < 7$ K was obtained in the case of non-magnetic La-doped $(\text{Ba}_{1-x}\text{La}_x)\text{Fe}_2\text{As}_2$ epitaxial films with maximum $T_c^{\text{onset}} = 22.4$ K [18], it seems that the doping of RE with $4f$ electrons decreases the SVF of its superconducting phases in the extreme. This result is markedly different from that in the case of the $(\text{Ca}_{1-x}\text{RE}_x)\text{Fe}_2\text{As}_2$ crystals because the maximum T_c^{onset} of the RE -doped CaFe_2As_2 single crystal increases in the order of $RE = \text{La, Ce, Pr and Nd}$, which is opposite to the present $(\text{Ba}_{1-x}\text{RE}_x)\text{Fe}_2\text{As}_2$ case [13–16].

D. Electronic phase diagrams

Figure 5 summarizes the electronic phase diagrams for the $(\text{Ba}_{1-x}\text{RE}_x)\text{Fe}_2\text{As}_2$ epitaxial films. The electronic phase diagram of $(\text{Ba}_{1-x}\text{La}_x)\text{Fe}_2\text{As}_2$ epitaxial films is also shown in the figure for comparison [18]. For all RE dopants, the antiferromagnetic

(AFM) transition at T_{anom} is suppressed as x_{film} increases, but the suppression rate of T_{anom} is different for different dopants; i.e., it decreases in the order of $RE = \text{La, Ce, Pr, and Nd}$. The vertical arrows, which indicate the extrapolated intersections at the x_{film} axis by using a phenomenological fit to T_{anom} , indicate this trend more clearly. The extrapolated x -point (critical x), where the resistivity anomaly would disappear completely, shifts to higher x_{film} values in the order of La-, Ce-, and Pr-doping (in the case of Nd doping, the extrapolation is unavailable because of the low solubility limit).

The plots of $T_{\text{c}}^{\text{onset}}$ for the $(\text{Ba}_{1-x}\text{Ce}_x)\text{Fe}_2\text{As}_2$ epitaxial films form a dome-shaped structure in the $0.06 \leq x_{\text{film}} \leq 0.28$ range. Also, in the cases of Pr- and Nd-doping, T_{c} appeared at $x_{\text{film}} > 0.1$ as T_{anom} shifted to the lower T side. However, unlike the Ce-doping case, neither of the superconducting domes extended to an over-doped region. The maximum $T_{\text{c}}^{\text{onset}}$ values for the $(\text{Ba}_{1-x}\text{Ce}_x)\text{Fe}_2\text{As}_2$ and $(\text{Ba}_{1-x}\text{Pr}_x)\text{Fe}_2\text{As}_2$ films were obtained at their critical x -points of ~ 0.15 and ~ 0.18 , respectively. The coexistence of superconductivity with an AFM state is stabilized only in the doping region that is lower than the critical x . The superconducting dome shape and the coexistence of AFM with superconductivity are qualitatively similar to those observed in the $(\text{Ba}_{1-x}\text{La}_x)\text{Fe}_2\text{As}_2$ epitaxial films, but the superconducting dome is slightly shifted to a higher x_{film} values and the height of the dome becomes smaller than that of $(\text{Ba}_{1-x}\text{La}_x)\text{Fe}_2\text{As}_2$, suggesting that the maximum $T_{\text{c}}^{\text{onset}}$ at the critical x point decreases depending on the RE dopant species. The difference in the suppression rate of T_{anom} and the superconducting dome shift may relate to the different variations in the c -axis lattice parameters with respect to x_{film} , as shown in Fig. 2(a). The inset figure in Fig. 5 replots T_{anom} and $T_{\text{c}}^{\text{onset}}$ against the c -axis lattice parameters for the $(\text{Ba}_{1-x}RE_x)\text{Fe}_2\text{As}_2$ epitaxial films. The suppression curves of T_{anom} converge to a single line, and the peak position of the superconducting

dome converges to the same c -axis length of 1.285 nm. This result implies that both chemical pressure and carrier doping are effective for suppression of the AFM transition and induction of superconductivity in the BaFe_2As_2 system [29].

4. Discussion

First, we should remind that the amounts of the Fe impurity in the $(\text{Ba}_{1-x}\text{RE}_x)\text{Fe}_2\text{As}_2$ films were almost the same in all the samples with the different RE dopants; therefore, the severe decrease in T_c and superconducting volume fractions cannot be explained by the impurity effects such as Fe. There are other plausible origins of the differences in the maximum T_c^{onset} and SVFs of the superconducting phase of the $(\text{Ba}_{1-x}\text{RE}_x)\text{Fe}_2\text{As}_2$ films with the different RE dopants. The first is the structural differences, because it has been noted that the shapes and sizes of the FeAs_4 tetrahedra critically affect the superconducting properties of iron pnictide superconductors; i.e. deviation of the As–Fe–As bonding angle from a regular tetrahedron is highly correlated with the maximum T_c values achieved [30]. Theoretical works have also shown that the Fermi surface topology is highly sensitive to the height of the As atom from the Fe sheet [31]. BaFe_2As_2 has a tetragonal crystal structure with a space group of $I4/mmm$, in which only the z -coordinate of the As (z_{As} , at the Wyckoff position $4e$) site is a variable parameter. The height of the As atom from the Fe sheet ($h_{\text{As}} = c(z_{\text{As}} - 0.25)$) and the As-Fe-As angle ($\alpha = 2\tan^{-1}(a/2h_{\text{As}})$) can therefore be estimated if the a -axis and c -axis lattice parameters and z_{As} are determined. It has been reported that z_{As} can be estimated from the ratio of the integrated intensities of $00l$ diffractions of epitaxial films in the out-of-plane XRD patterns [32]. In the Ce-doping case, it was found that z_{As} only changed from $z_{\text{As}} = 0.3545$ at $x = 0$ to 0.352, even when $x_{\text{film}} = 0.29$, because the intensity

ratios of the $00l$ diffractions showed little change, as shown in Fig. 1(a), which indicates that the angle α and h_{As} primarily depend on the lattice parameters [33]. Table I summarizes the superconducting and structural parameters of the following optimally doped epitaxial films with critical x : $(Ba_{0.87}La_{0.13})Fe_2As_2$ with maximum T_c^{onset} of 22.4 K, $(Ba_{0.85}Ce_{0.15})Fe_2As_2$ with T_c^{onset} of 13.4 K, and $(Ba_{0.82}Pr_{0.18})Fe_2As_2$ with T_c^{onset} of 6.2 K. The lattice parameters and the structural parameters, such as z_{As} , h_{As} , and the α angles, are almost the same for each dopant. Density functional structure relaxation calculations for the models of $(Ba_{3/4}RE_{1/4})Fe_2As_2$ supported this result in that there is no remarkable difference in z_{As} , h_{As} , and the α angles for different RE dopants. These results indicate that the difference in the maximum T_c and the SVFs of the superconducting phases cannot be explained in terms of difference in the local structure.

Another plausible origin is the different electronic properties that originate from the different numbers of the RE $4f$ electrons. It should be noted that the ρ - T curves in Fig. 3 have a minimum at T_{min} (shown by closed triangles) and that the resistivities show an upturn in the T region lower than T_{min} for the $(Ba_{1-x}RE_x)Fe_2As_2$ epitaxial films with x_{film} larger than the critical x . We used conventional power-law behavior, where $\rho = \rho_0 + AT^n$ (where ρ_0 is the residual resistivity), for these ρ - T curves at $T > T_{\text{min}}$ to evaluate the electron scattering. The fitting results, indicated by the black lines in Fig. 3, agree well with the experimental ρ - T curves. The resistivity upturn can be explained either by carrier localization with disorder scattering [34] or by magnetic scattering [35]. Therefore, the origin of the weak resistivity-upturn behavior for the non-magnetic La-doping should lie in carrier localization induced by defects and/or disorders generated by the large difference in ion radii between Ba^{2+} and La^{3+} , which causes local structural distortions. Because the resistivity upturn at $<T_{\text{min}}$ is very weak in the case of

the non-magnetic La dopant, this indicates that the extra resistivity upturns for $RE = \text{Ce}$ and Pr originate from magnetic scattering caused by the magnetic RE dopants. Therefore, a possible mechanism for breaking of the superconducting electron-pair is the interaction between the localized RE $4f$ electrons and the Fe $3d$ conduction electrons [36]. The contribution of the magnetic RE ions to the electron scattering can be estimated by comparing the electronic properties of the RE -doped samples with those of the nonmagnetic reference $(\text{Ba}_{1-x}\text{La}_x)\text{Fe}_2\text{As}_2$ epitaxial films, because their structural differences are negligible, as shown in Fig. 2 and Table I.

The excess resistivity caused by a magnetic scattering should give rise to a negative magnetoresistance (MR), because a high magnetic field suppresses spin inversion and scattering [35]. To clarify the magnetic scattering behavior, the field dependence of MR, which is defined as $[\rho(\mu_0 H) - \rho(0)]/\rho(0) \times 100$, was measured at 30 K under fields of up to $\mu_0 H = 9$ T applied parallel to the c -axis and at the DC-current in the ab -plane of the epitaxial film. Figure 6(a–c) shows the MR for epitaxial films of $(\text{Ba}_{1-x}\text{La}_x)\text{Fe}_2\text{As}_2$ with $x_{\text{film}} = 0\text{--}0.44$, $(\text{Ba}_{1-x}\text{Ce}_x)\text{Fe}_2\text{As}_2$ with $x_{\text{film}} = 0.06\text{--}0.29$, and $(\text{Ba}_{1-x}\text{Pr}_x)\text{Fe}_2\text{As}_2$ with $x_{\text{film}} = 0.06\text{--}0.18$. No asymmetry against negative fields and hysteresis were observed in the cyclic measurements. The MR of the undoped BaFe_2As_2 epitaxial films, shown in Fig. 6(a), showed a large positive MR up to +15% at $\mu_0 H = 9$ T. Similar to the results of a previous report on undoped BaFe_2As_2 single crystals [37, 38], the MR of the undoped BaFe_2As_2 epitaxial film does not follow the standard Kohler's rule with H^2 dependence, and the crossover from the H^2 dependence at lower fields to the linear dependence at higher fields is observed at $\mu_0 H = 6.3$ T. The observed MR can be fitted well by a modified two-band galvanomagnetic model (MR_{SDW}) [39], in which the positive MR is caused by a magnetically ordered state that originates from

spin-density-wave (SDW) gaps at low temperatures $< T_{\text{anom}}$. The MR_{SDW} is expressed by $\Delta\rho/\rho_0 = 4(\beta - \gamma H)\mu_0^2 H^2 [(1 + \beta - \gamma H)^2 + (1 - \beta + \gamma H)^2 \mu_0^2 H^2]^{-1}$, where β is the ratio of the itinerant majority carrier concentration to the minority carrier concentration at $\mu_0 H = 0$ T, γ is a constant value representing the magnetic field effect on the ratio of carrier concentration, and μ_0 is the mobility of majority carriers, respectively. In the case of the non-magnetic La doping, the positive MR decreases with the increase in x_{film} and disappears at the critical x of 0.13. All of the positive MR observed on the La-doped films is explained very well by the MR_{SDW} model, as shown by the fitting curves in Fig. 6(a). The fitted parameters are summarized in Table 2. The β values increase and μ_0 decrease with increasing the x_{film} , while γ values remain constant, which is consistent with the La-doping result that the La-doping increased the majority carriers (electrons) and decreased their mobilities. The MR became undetectable at higher x_{film} values of 0.13–0.44, which is similar to the behavior of $\text{Ba}(\text{Fe}_{1-x}\text{Co}_x)_2\text{As}_2$ single crystals [40]. On the other hand, in the cases of magnetic Ce- and Pr-doping, a negative MR appeared as x_{film} increased. It has been reported that MR with magnetic scattering represents a $-H^2$ dependence at low fields, and it then follows a $-\log H$ dependence after sufficient suppression of the spin inversion [41,42]. It is seen that carrier doping into the BaFe_2As_2 films by the non-magnetic La dopants generate MR_{SDW} only, while negative MR expressed by $-H^2$ and $-\log H$ are superimposed for the magnetic Ce- and Pr-doping cases. The fitting results are shown by the curves in Figs. 6(b) and (c). The coexistence of a positive MR and a weak negative MR with $-H^2$ dependence was observed for low $x_{\text{film}} < 0.12$. With an increase in x_{film} , the positive MR disappeared and only the negative MR was then observed. In the case of Ce-doping with x_{film} up to 0.18, the negative MR showed a $-H^2$ dependence at fields up to 9 T. The MR at larger values of x_{film} up to 0.29

deviates from the $-H^2$ dependence at a higher value of $\mu_0 H$ of 3 T and showed a transition to the $-\log H$ dependence. With decrease in temperature from 30 K to 2 K, the negative MR becomes larger and the transition H value from the $-H^2$ dependence to the $-\log H$ dependence shifts to lower fields (see supplementary Fig. S4 for MR measured at 30, 10, and 2 K for $(\text{Ba}_{0.72}\text{Ce}_{0.28})\text{Fe}_2\text{As}_2$ epitaxial film). In addition, the negative MR along the ab -plane is much smaller than that along the c -axis. This result indicates that antiferromagnetic spin-ordering parallel to the c -axis and ferromagnetic ordering parallel to the ab -plane affect the negative MR (see supplementary Fig. S4). Also, in the Pr-doping case, the field dependence changed from $-H^2$ to $-\log H$ in the negative MR observed at a high $\mu_0 H$ of 2.5 T, even at a low x_{film} value of 0.18. With an increase in the numbers of $4f$ electrons from the RE dopants, the negative MR increased (the observed maximum negative MR = -0.15% for the Ce doping and -0.42% for the Pr doping with the same x_{film} value of 0.18.) No observation of the negative MR in the $(\text{Ba}_{1-x}\text{La}_x)\text{Fe}_2\text{As}_2$ films and the enhanced negative MR in the Ce- and Pr-doping cases, which is associated with spin flip magnetic scattering of the charge carriers, indicate that the interaction between the $4f$ electrons and the conduction $3d$ electrons is enhanced in the order from Ce- to Pr-doping. This would cause the electron pair-breaking that is responsible for the suppression of superconductivity in the magnetic RE -ion doped $(\text{Ba}_{1-x}\text{RE}_x)\text{Fe}_2\text{As}_2$ epitaxial films.

As noted at the last of section 3 C, the variation of T_c with the RE dopant is opposite between the present $(\text{Ba}_{1-x}\text{RE}_x)\text{Fe}_2\text{As}_2$ epitaxial films and the $(\text{Ca}_{1-x}\text{RE}_x)\text{Fe}_2\text{As}_2$ single crystals; i.e., the maximum T_c of the $(\text{Ba}_{1-x}\text{RE}_x)\text{Fe}_2\text{As}_2$ epitaxial films decreases in the order of $RE = \text{La}, \text{Ce}, \text{Pr}$ and Nd , while that of the $(\text{Ca}_{1-x}\text{RE}_x)\text{Fe}_2\text{As}_2$ single crystals increases in this order [13–16]. The origins of this difference would be

classified to an intrinsic effect and an extrinsic effect. To clarify the extrinsic effect originating from the different crystal structure parameters and crystalline quality between the thin films and the single crystals, we should use epitaxial films of *RE*-doped CaFe_2As_2 epitaxial films; however, unfortunately, epitaxial thin film growth of CaFe_2As_2 by PLD has not been attained [21]. Here, we like to discuss plausible intrinsic origins. One possible origin of this discrepancy may be the structural transition in $(\text{Ca}_{1-x}\text{RE}_x)\text{Fe}_2\text{As}_2$. It should be noted that $(\text{Ca}_{1-x}\text{RE}_x)\text{Fe}_2\text{As}_2$ transits easily to a collapsed tetragonal structure by replacing the Ca site with a smaller *RE* dopant, such as Pr and Nd [13]. In the thin film samples used here, the local structures of the $(\text{Ba}_{1-x}\text{RE}_x)\text{Fe}_2\text{As}_2$ films remained almost unchanged for different *RE*, implying that the film's electronic structures are not changed drastically by the *RE* doping. Therefore, it would be possible that the structural flexibility to a collapsed structure in $(\text{Ca}_{1-x}\text{RE}_x)\text{Fe}_2\text{As}_2$ contributes to the high T_c .

5. Conclusions

A non-equilibrium PLD process was used to stabilize nonmagnetic/magnetic *RE* (= La, Ce, Pr, and Nd) dopants in BaFe_2As_2 and their superconductivity were examined with respect to the $4f$ electrons of *RE* dopants. The indirect electron doping of each *RE* element produced superconductivity along with a suppression of the resistivity anomaly, which is associated with the magnetic/structural phase transitions. The La- and Ce-doping induced bulk superconductivity at a maximum T_c^{onset} of 22.4 K at $x_{\text{film}} = 0.13$ for La doping and 13.4 K at $x_{\text{film}} = 0.15$ for Ce doping, respectively. In the cases of Pr- and Nd-doping, the superconducting transitions started from $T_c^{\text{onset}} = 6.2$ K and 5.8 K, respectively, while zero resistivity and diamagnetism were not observed. The severe

decrease in T_c^{onset} and SVFs upon *RE*-doping from non-magnetic La to magnetic Ce and Pr are attributed to magnetic electron pair breaking, as evidence of the magnetic electron scattering and the negative MR, with interaction between the localized $4f$ electrons and the Fe $3d$ conduction electrons.

References

- [1] Kamihara Y, Watanabe T, Hirano M and Hosono H 2008 *J. Am. Chem. Soc.* **130** 3296.
- [2] Rotter M, Tegel M and Johrendt D 2008 *Phys. Rev. Lett.* **101** 107006
- [3] Sefat A S, Jin R, McGuire M A, Sales B C, Singh D J and Mandrus D 2008 *Phys. Rev. Lett.* **101** 117004
- [4] Singh D J and Du M H 2008 *Phys. Rev. Lett.* **100** 237003
- [5] Ren Z A, Lu W, Yang J, Yi W, Shen X L, Li Z C, Che G C, Dong X L, Sun L L, Zhou F and Zhao Z X 2008 *Chin. Phys. Lett.* **25** 2215
- [6] Wang C, Li Y K, Zhu Z W, Jiang S, Lin X, Luo Y K, Chi S, Li L J, Ren Z, He M, Chen H, Wang Y T, Tao Q, Cao G H and Xu Z A 2009 *Phys. Rev. B* **79** 054521
- [7] Ni N, Tillman M E, Yan J Q, Kracher A, Hannahs S T, Bud'ko S L and Canfield P. C 2008 *Phys. Rev. B* **78** 214515
- [8] Jiang S, Xing H, Xuan G, Wang C, Ren Z, Feng C, Dai J, Xu Z and Cao G 2009 *J. Phys.: Condens. Matter* **21** 382203
- [9] Wu G, Liu R H, Chen H, Yan Y J, Wu T, Xie Y L, Ying J J, Wang X F, Fang D F and Chen X H 2008 *Europhys. Lett.* **84** 27010
- [10] Muraba Y, Matsuishi S, Kim S W, Atou T, Fukunaga O and Hosono H 2010 *Phys. Rev. B* **82** 180512
- [11] Leithe-Jasper A, Schnelle W, Geibel C and Rosner H 2008 *Phys. Rev. Lett.* **101** 207004
- [12] Kasinathan D, Ormeci A, Koch K, Burkhardt U, Schnelle W, Leithe-Jasper A and Rosner H 2009 *New J. Phys.* **11** 025023
- [13] Saha S R, Butch N P, Drye T, Magill J, Ziemak S, Kirshenbaum K, Zavalij P Y, Lynn J W and Paglione J 2012 *Phys. Rev. B* **85** 024525
- [14] Lv B, Deng L, Gooch M, Wei F, Sun Y, Meen J K, Xue Y Y, Lorenz B and Chu C W 2011 *Proc. Natl. Acad. Sci. USA* **108** 15705
- [15] Gao Z, Qi Y, Wang L, Wang D, Zhang X, Yao C, Wang C and Ma Y 2011 *Europhys. Lett.* **95** 67002
- [16] Qi Y, Gao Z, Wang L, Wang D, Zhang X, Yao C, Wang C, Wang C and Ma Y 2012 *Supercond. Sci. Technol.* **25** 045007

- [17] Shannon R D 1976 *Acta Crystallogr. A* **32** 751
- [18] Katase T, Iimura S, Hiramatsu H, Kamiya T and Hosono H 2012 *Phys. Rev. B* **85** 140516
- [19] Hiramatsu H, Katase T, Kamiya T and Hosono H 2012 *J. Phys. Soc. Jpn.* **81** 011011
- [20] Katase T, Hiramatsu H, Kamiya T and Hosono H 2010 *Appl. Phys. Express* **3** 063101
- [21] Katase T, Hiramatsu H, Kamiya T and Hosono H 2012 *Supercond. Sci. Technol.* **25** 084015
- [22] Hulliger F 1979 “Handbook of the Physics and Chemistry of Rare Earths”, ed. by K. A. Gschneidner, Jr., L. Eyring, North-Holland, New York, Vol. 4, p. 158.
- [23] Huang Q, Qiu Y, Bao W, Green M A, Lynn J W, Gasparovic Y C, Wu T, Wu G and Chen X H 2008 *Phys. Rev. Lett.* **101** 257003
- [24] Morinaga R, Matan K, Suzuki H S and Sato T J 2009 *Jpn. J. Appl. Phys.* **48** 013004
- [25] Mani A, Ghosh N, Paulraj S, Bharathi A and Sundar C S 2009 *Europhys. Lett.* **87** 17004
- [26] Chu J H, Analytis J G, De Greve K, McMahon P L, Islam Z, Yamamoto Y and Fisher I R 2010 *Science* **329** 824
- [27] Maiorov B, Katase T, Baily S A, Hiramatsu H, Holesinger T G, Hosono H and Civale L 2011 *Supercond. Sci. Technol.* **24** 055007
- [28] Sato H, Katase T, Kang W N, Hiramatsu H, Kamiya T and Hosono H 2013 *Phys. Rev. B* **87** 064504
- [29] Colombier E, Bud’ko S L, Ni N and Canfield P C 2009 *Phys. Rev. B* **79** 224518
- [30] Lee C H, Iyo A, Eisaki H, Kito H, Fernandez-Diaz M T, Ito T, Kihou K, Matsuhata H, Braden M and Yamada K 2008 *J. Phys. Soc. Jpn.* **77** 083704
- [31] Kuroki K, Usui H, Onari S, Arita R and Aoki H 2009 *Phys. Rev. B* **79** 224511
- [32] Huang S X, Chien C L, Thampy V and Broholm C 2010 *Phys. Rev. Lett.* **104** 217002
- [33] Johnston D C 2010 *Adv. Phys.* **59** 803
- [34] Lee P A and Ramakrishnan T V 1985 *Rev. Mod. Phys.* **57** 287
- [35] Alloul H, Bobroff J, Gabay M and Hirschfeld P J 2009 *Rev. Mod. Phys.* **81** 45
- [36] Abrikosov A A and Gor’kov L P 1961 *JETP* **12** 1243

- [37] Kuo H H, Chu J H, Riggs S C, Yu L, McMahon P L, De Greve K, Yamamoto Y, Analytis J G and Fisher I R 2011 *Phys. Rev. B* **84** 054540
- [38] Huynh K K, Tanabe Y and Tanigaki K 2011 *Phys. Rev. Lett.* **106** 217004
- [39] Zheng P, Chen G F, Li Z, Hu W Z, Dong J, Li G, Wang N L and Luo J L 2009 *Chin. Phys. Lett.* **26** 107401
- [40] Vinod K, Satya A T, Sharma S, Sundar C S and Bharathi A 2011 *Phys. Rev. B* **84** 012502
- [41] Yatskar A, Mielke C H, Canfield P C, Lacerda A H and Beyermann W P 1999 *Phys. Rev. B* **60** 8012
- [42] Whitney D A, Fleming R M and Coleman R V 1977 *Phys. Rev. B* **15** 3405

Acknowledgment

This work was supported by the Japan Society for the Promotion of Science (JSPS), Japan, through the “Funding Program for World-Leading Innovative R&D on Science and Technology (FIRST Program)” and MEXT Element Strategy Initiative to Form Core Research Center.

Figure captions

Figure 1. High-resolution out-of-plane XRD patterns for films of $(\text{Ba}_{1-x}\text{Ce}_x)\text{Fe}_2\text{As}_2$ (a), $(\text{Ba}_{1-x}\text{Pr}_x)\text{Fe}_2\text{As}_2$ (b), $(\text{Ba}_{1-x}\text{Nd}_x)\text{Fe}_2\text{As}_2$ (c), and Sm-containing BaFe_2As_2 (d) with various x_{film} values. The x_{film} value is shown on the upper right of each panel. The vertical dashed lines indicate the 00 ℓ diffraction angles of the undoped BaFe_2As_2 phase. The asterisks show the 110 diffraction peaks from the Fe impurity phase.

Figure 2. x_{film} dependence of structural properties of $(\text{Ba}_{1-x}\text{RE}_x)\text{Fe}_2\text{As}_2$ epitaxial films. (a) a -axis and c -axis lattice parameters and unit cell volume V , (b) FWHM values of rocking curves for 004 ($\Delta\omega$) and 200 ($\Delta\phi$) diffractions, and (c) FWHM values of 004 diffractions ($\Delta 2\theta$). The solid lines in the middle figure of (a) are indicators of changes in the c -axis lattice parameters. Open pentagon symbols and dotted lines show the results for undoped BaFe_2As_2 films. The diamonds, circles, squares, and triangles indicate values for La-, Ce-, Pr-, and Nd-doped films, respectively.

Figure 3. ρ - T curves in the temperature range from 300 to 2 K for (a) $(\text{Ba}_{1-x}\text{Ce}_x)\text{Fe}_2\text{As}_2$ ($x_{\text{film}}=0$ –0.29), (b) $(\text{Ba}_{1-x}\text{Pr}_x)\text{Fe}_2\text{As}_2$ ($x_{\text{film}}=0.06$ –0.18), and (c) $(\text{Ba}_{1-x}\text{Nd}_x)\text{Fe}_2\text{As}_2$ ($x_{\text{film}}=0.07$ –0.13) epitaxial films, respectively. The doping concentration x_{film} is indicated on the upper left of each panel. The inset figures show magnified views around T_c . The arrows and triangles indicate the positions of T_{anom} and T_{min} , respectively. The black curved lines are fitting results from conventional power-law behavior, $\rho = \rho_0 + AT^n$ (ρ_0 : residual resistivity), in the higher-temperature regions.

Figure 4. ρ - T curves under magnetic fields of 0–9 T for optimally doped

(Ba_{0.85}Ce_{0.15})Fe₂As₂ (a), (Ba_{0.82}Pr_{0.18})Fe₂As₂ (b), and (Ba_{0.87}Nd_{0.13})Fe₂As₂ (c) epitaxial films. The inset figures show χ - T curves under a magnetic field of 5 G.

Figure 5. Electronic phase diagrams of (Ba_{1-x}RE_x)Fe₂As₂ epitaxial films. The diamonds, circles, squares, and triangles represent phase diagrams for the epitaxial films of (Ba_{1-x}La_x)Fe₂As₂ [18], (Ba_{1-x}Ce_x)Fe₂As₂, (Ba_{1-x}Pr_x)Fe₂As₂, and (Ba_{1-x}Nd_x)Fe₂As₂, respectively. T_{anom} and $T_{\text{c}}^{\text{onset}}$ are indicated by the closed and open symbols, respectively. The vertical dashed/dotted lines indicate the solubility limits for the dopants. The dashed curves show phenomenological fits to T_{anom} as a function of x_{film} , and the bottom vertical arrows indicate the critical x points extrapolated to $T_{\text{anom}}=0$. The inset figure represents the c -axis lattice parameter dependences of T_{anom} and $T_{\text{c}}^{\text{onset}}$.

Figure 6. Field dependence of magnetoresistance $\text{MR} = [\rho(\mu_0 H) - \rho(0)]/\rho(0) \times 100$ at 30 K for epitaxial films of (a) (Ba_{1-x}La_x)Fe₂As₂ with $x_{\text{film}}=0-0.44$, (b) (Ba_{1-x}Ce_x)Fe₂As₂ with $x_{\text{film}}=0.06-0.29$, and (c) (Ba_{1-x}Pr_x)Fe₂As₂ with $x_{\text{film}}=0.06-0.18$. The x_{film} values for each MR are indicated in the figures. The solid red lines in (a) represent the fitting results with the MR_{SDW} model, and those in (b) and (c) show the fitting results with a $\text{MR}_{\text{SDW}} - \alpha H^2$ model. The dotted lines in (b) and (c) indicate the fitting results with a $\text{MR}_{\text{SDW}} - \beta \log H + \text{const.}$ and the arrows represent the transition point from a $-\alpha H^2$ dependence to a $-\alpha \log H$ dependence.

Table. I. Summary of superconducting and structural properties of optimally doped epitaxial films of (Ba_{0.87}La_{0.13})Fe₂As₂, (Ba_{0.85}Ce_{0.15})Fe₂As₂, and (Ba_{0.82}Pr_{0.18})Fe₂As₂.

Table. II. Summary of the fitting parameters using the model [39] for the magnetoresistance of $(\text{Ba}_{1-x}\text{La}_x)\text{Fe}_2\text{As}_2$ epitaxial films. Errors are indicated in the values in the parentheses.

Figures

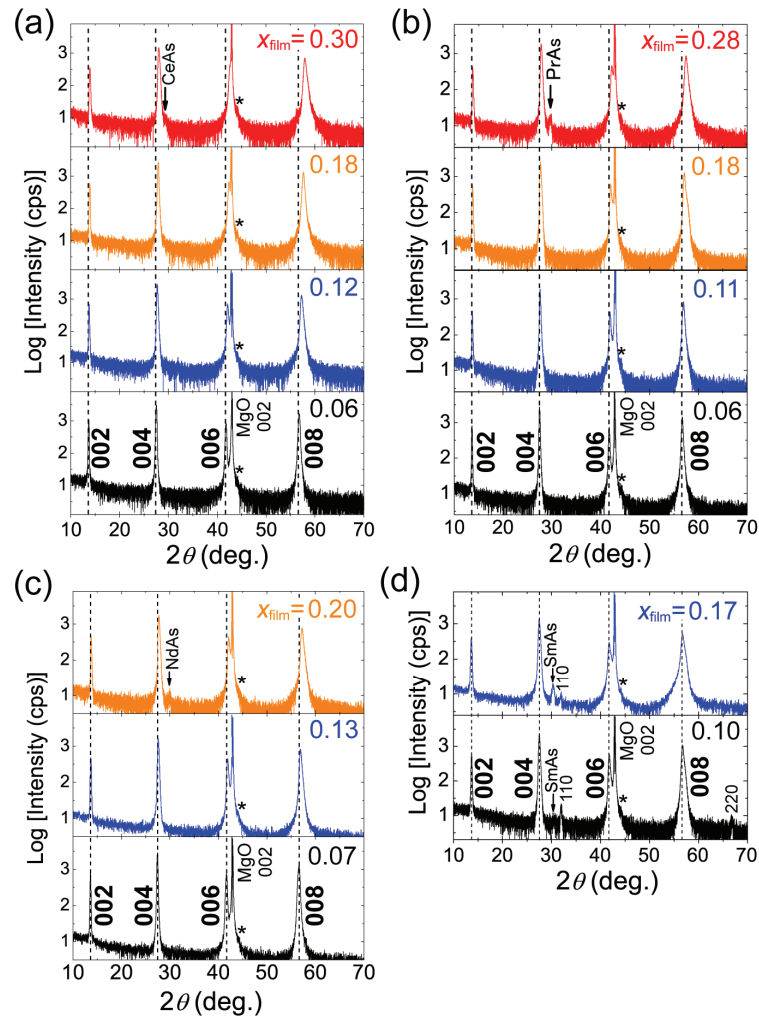


Figure 1.

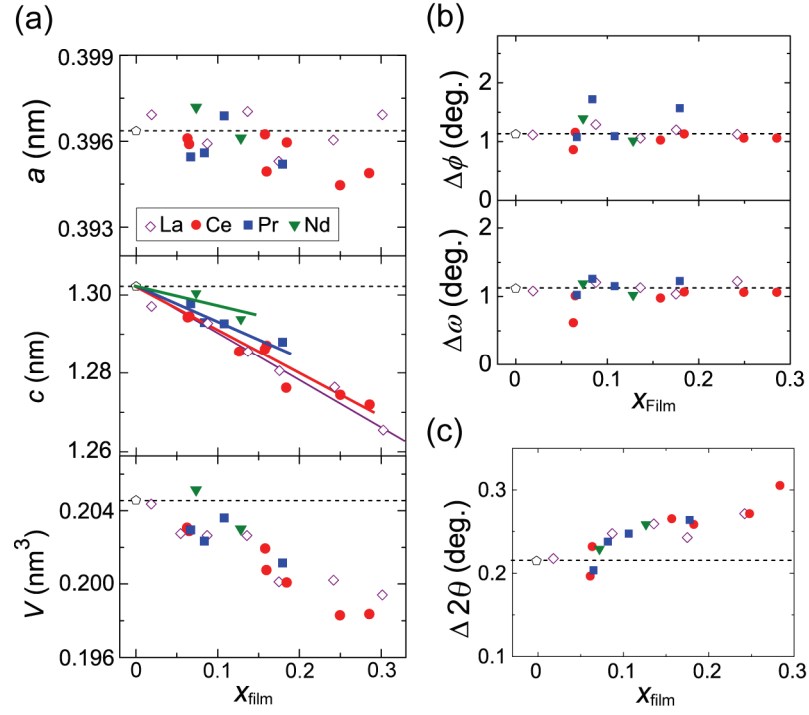


Figure 2.

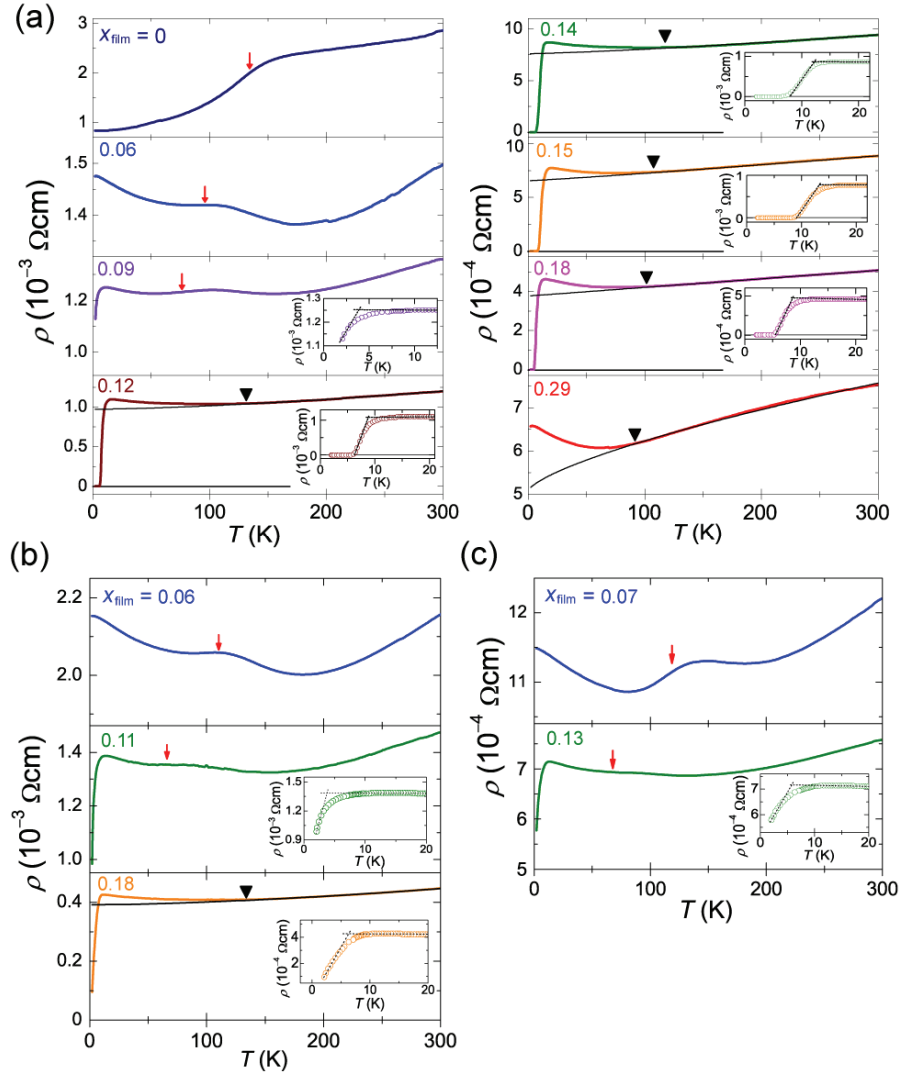


Figure 3.

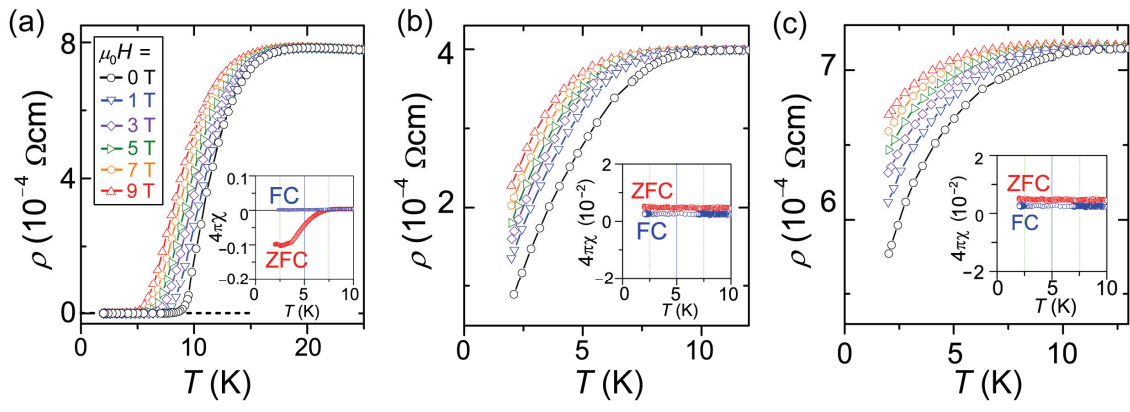


Figure 4.

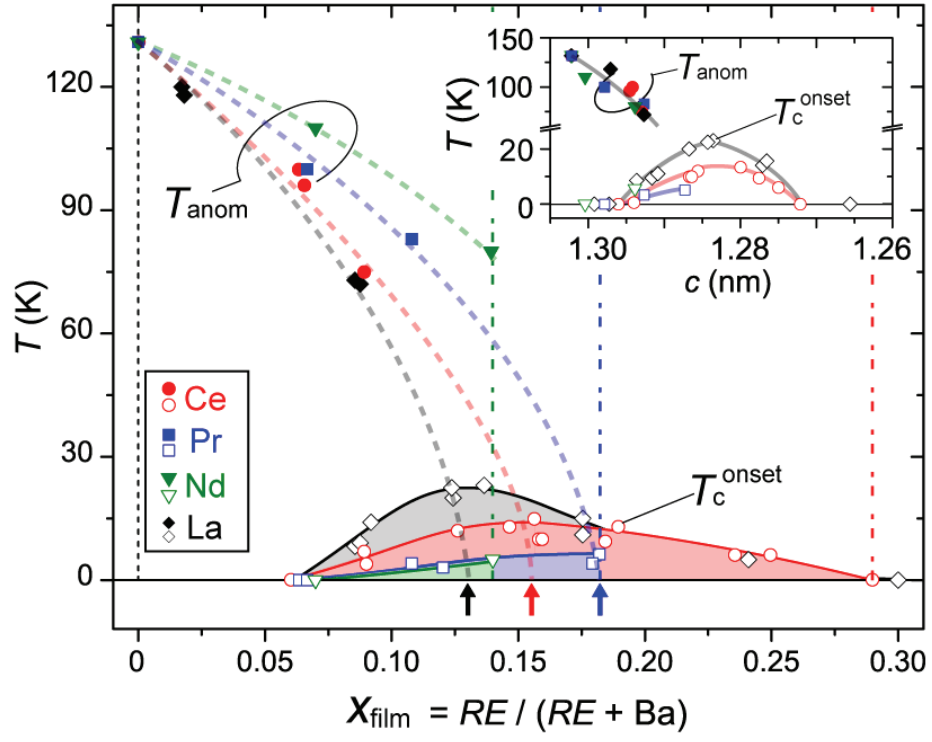


Figure 5.

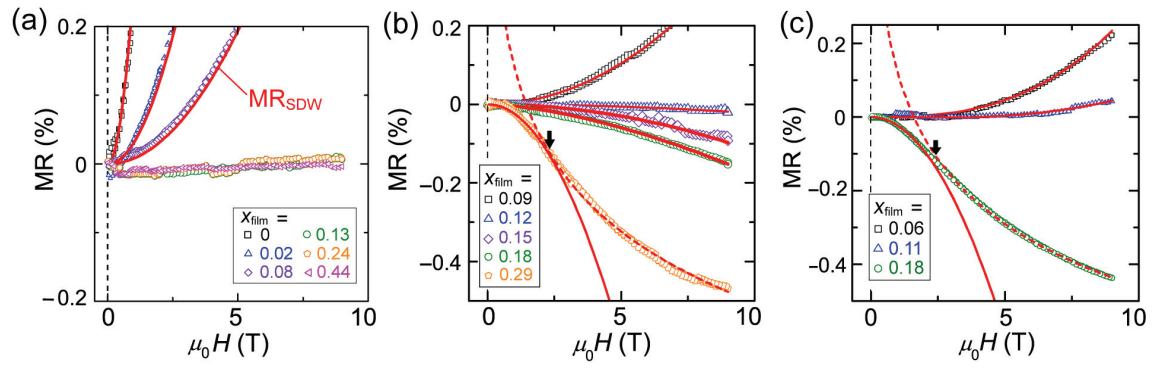


Figure 6.

Table 1.

	Optimal x_{film}	$T_{\text{c}}^{\text{onset}}$ (K)	c (nm)	a (nm)	z_{As}	h_{As} (nm)	α (deg.)
$(\text{Ba}_{1-x}\text{La}_x)\text{Fe}_2\text{As}_2$	0.13	22.4	1.2872	0.3970	0.352	0.13129	113.04
$(\text{Ba}_{1-x}\text{Ce}_x)\text{Fe}_2\text{As}_2$	0.15	13.4	1.2866	0.3962	0.352	0.13123	112.95
$(\text{Ba}_{1-x}\text{Pr}_x)\text{Fe}_2\text{As}_2$	0.18	6.2	1.2879	0.3952	0.352	0.13136	112.76

Table 2.

	T	β	γ	μ_0 (m ² /Vs)
$x_{\text{film}} = 0$ in (Ba _{1-x} La _x)Fe ₂ As ₂ film	30	34.0 (± 0.1)	1.75 (± 0.05)	0.151 (± 0.001)
$x_{\text{film}} = 0.02$ in (Ba _{1-x} La _x)Fe ₂ As ₂ film	30	79.0 (± 0.3)	1.25 (± 0.06)	0.0740 (± 0.001)
$x_{\text{film}} = 0.08$ in (Ba _{1-x} La _x)Fe ₂ As ₂ film	30	98.7 (± 0.8)	1.52 (± 0.06)	0.0430 (± 0.0004)
BaFe ₂ As ₂ single crystal (Ref. 39)	50	44.5	1.14	0.16

Supplementary Information for
**“Magnetic scattering and electron pair breaking by rare-earth-ion substitution in
 BaFe₂As₂ epitaxial films”**

Takayoshi Katase^{1,4}, Hidenori Hiramatsu^{2,3}, Toshio Kamiya^{2,3} and Hideo Hosono^{1,2,3,5}

¹ Frontier Research Center, Tokyo Institute of Technology, S2-6F East, 4259 Nagatsuta-cho, Midori-ku, Yokohama 226-8503, Japan

² Materials and Structures Laboratory, Tokyo Institute of Technology, 4259 Nagatsuta-cho, Midori-ku, Yokohama 226-8503, Japan

³ Materials Research Center for Element Strategy, Tokyo Institute of Technology, 4259 Nagatsuta-cho, Midori-ku, Yokohama 226-8503, Japan

⁴ Present address: Research Institute for Electronic Science, Hokkaido University, Sapporo 001-0020, Japan

⁵ Corresponding author. E-mail: hosono@msl.titech.ac.jp

I. Synthesis of bulk polycrystal samples of rare earth (*RE*) containing BaFe₂As₂

Bulk polycrystal samples of *RE*- (= Ce, Pr, Nd, and Sm) containing BaFe₂As₂ were synthesized for the PLD targets by two-step solid-state reactions. All preparation procedures except for the annealing process were carried out in an Ar-filled glove box (the O₂ impurity concentration was < 1 ppm and the dew point was < −100°C). A mixture of fine pieces of Ba and *RE* metals along with the powders of Fe and As were mixed in a stoichiometric atomic ratio of Ba : *RE* : Fe : As = 1−*x* : *x* : 2 : 2 and sealed in a stainless-steel tube under a pure Ar atmosphere, followed by a reaction at 700°C for 10 h. The resulting powders were grounded thoroughly and pressed into pellets. The pellets were placed in stainless-steel tubes and heated at 900°C for 16 h. It is important to carefully avoid contamination with atmospheric impurities such as oxygen- and water-related molecules in the PLD targets in order to obtain the high-purity (Ba_{1−*x*}*RE*_{*x*})Fe₂As₂ films; i.e., we could not succeed in the *RE* doping at the early stages of this study when a small amount of a *REFeAsO* impurity phase was observed in the PLD targets. Further, it should be noted that the *REFeAsO* phase was always produced when we synthesized (Ba_{1−*x*}*RE*_{*x*})Fe₂As₂ using an agate mortar and evacuated silica glass tubes similar to the case to synthesize Ba(Fe,Co)₂As₂ in ref. S1. We, therefore, used a fully-dried silica-glass mortar to mix the powders and then sealed the pressed pellets into stainless tubes before the reactions.

Powder X-ray diffraction (XRD; anode radiation: $\text{CuK}\alpha$, D8 ADVANCE-TXS, Bruker AXS) was measured at room temperature for the resulting bulk polycrystals. Powder XRD patterns of the $(\text{Ba}_{1-x}\text{RE}_x)\text{Fe}_2\text{As}_2$ bulk polycrystal samples with nominal $x = 0.1$ are shown in Fig. S1(a), and the nominal x dependence of the lattice parameters in Fig. S1(b). No peak shift was observed in the diffraction angles of the $(\text{Ba}_{1-x}\text{RE}_x)\text{Fe}_2\text{As}_2$ samples from the calculated peak positions of undoped BaFe_2As_2 . The lattice shrinkage, which is considered to originate from the substitution of Ba with the *RE* ions having smaller ion radii, was not observed, even though x was varied up to 0.25. Simultaneously, the 200 diffractions for *REAs* impurities were observed distinctly for all the cases as indicated by the arrows in Fig. S1(a). These phase-separated bulk polycrystals (i.e., $\text{BaFe}_2\text{As}_2 + \text{REAs}$) were used as the PLD targets.

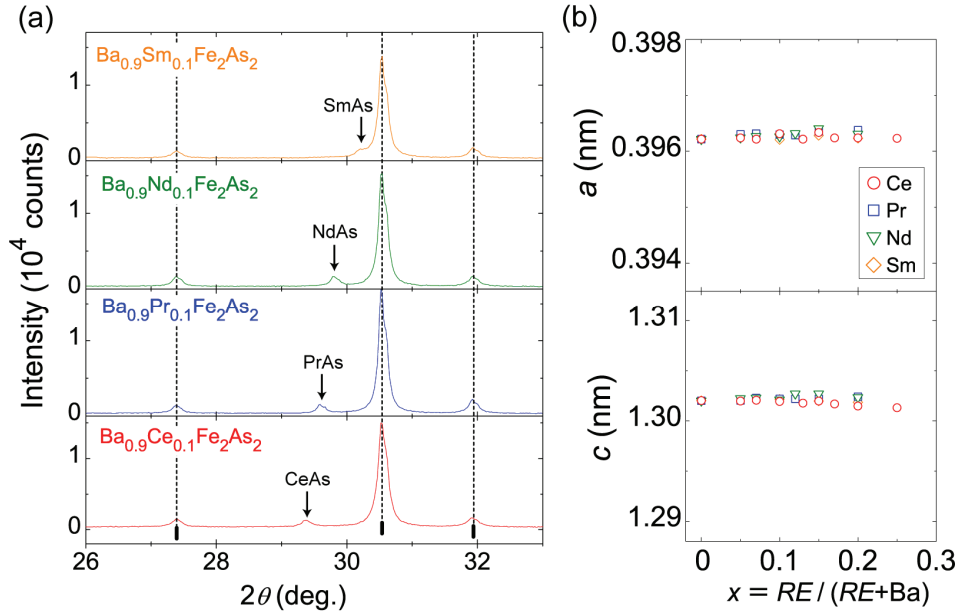


Figure S1. (a) Powder XRD patterns of $(\text{Ba}_{1-x}\text{RE}_x)\text{Fe}_2\text{As}_2$ bulk polycrystal samples with $x = 0.1$. The nominal chemical composition of the bulk crystal is indicated on upper left in each pattern. The vertical dotted lines indicate the diffraction angles of undoped BaFe_2As_2 . (b) The nominal x dependence of the a - and c -axis lattice parameters for the $(\text{Ba}_{1-x}\text{RE}_x)\text{Fe}_2\text{As}_2$ bulk polycrystal samples. The circle, square, triangle, and diamond symbols correspond to the results of the Ce, Pr, Nd, and Sm containing BaFe_2As_2 , respectively.

II. Chemical composition analysis of $(\text{Ba}_{1-x}\text{RE}_x)\text{Fe}_2\text{As}_2$ epitaxial films

Figure S2(a) shows the *RE* chemical composition mapping images for the optimally doped epitaxial films of $(\text{Ba}_{0.85}\text{Ce}_{0.15})\text{Fe}_2\text{As}_2$, $(\text{Ba}_{0.82}\text{Pr}_{0.18})\text{Fe}_2\text{As}_2$, and

(Ba_{0.87}Nd_{0.13})Fe₂As₂ examined with an electron-probe microanalyzer (EPMA). The EPMA mapping images ensured homogeneous *RE* distribution. Figure S2(b) presents the measured doping concentration x_{film} in the (Ba_{1-x}RE_x)Fe₂As₂ epitaxial films measured by EPMA as a function of the nominal x . The good linearity in the relationship between the measured x and the nominal x demonstrates that the chemical compositions of the PLD targets were transferred linearly to the films. The solubility limit lines, which shifted to lower x_{film} as *RE* changes in the order of Ce, Pr, and Nd, were determined as the chemical composition region where an impurity phase was not detected by the XRD measurements in Fig. 1.

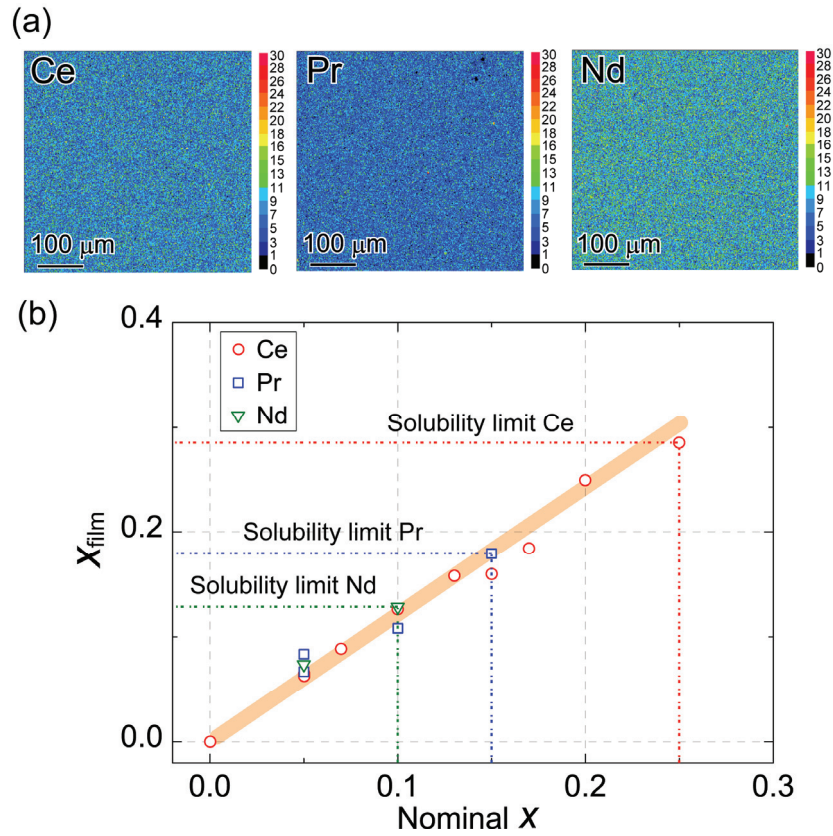


Figure S2 (a) EPMA mapping images of *RE* elements in epitaxial films of (Ba_{0.85}Ce_{0.15})Fe₂As₂ (left), (Ba_{0.82}Pr_{0.18})Fe₂As₂ (middle), and (Ba_{0.87}Nd_{0.13})Fe₂As₂ (right). The horizontal bars at bottom left in the maps indicate a 100 μm scale, and the numbers on right of the color scale bars indicate the measured signal intensity in counts per pixel. (b) Relationship between the x_{film} and the nominal x measured by EPMA. The circle, square, and triangle symbols indicate Ce-, Pr-, and Nd-doping results, respectively. The dotted lines represent the solubility limits.

III. Temperature derivative of resistivity

Figure S3 shows the temperature derivatives of resistivities ($d\rho/dT$) for the films in Fig. 3 [i.e., $(\text{Ba}_{1-x}\text{Ce}_x)\text{Fe}_2\text{As}_2$ with $x_{\text{film}} = 0-0.12$, $(\text{Ba}_{1-x}\text{Pr}_x)\text{Fe}_2\text{As}_2$ with $x_{\text{film}} = 0-0.18$, and $(\text{Ba}_{1-x}\text{Nd}_x)\text{Fe}_2\text{As}_2$ with $x_{\text{film}} = 0-0.13$]. The resistivity anomaly temperature (T_{anom}), defined as the peak position in the $d\rho/dT$ curves, shifts to lower T with increasing the doping concentrations (x_{film}).

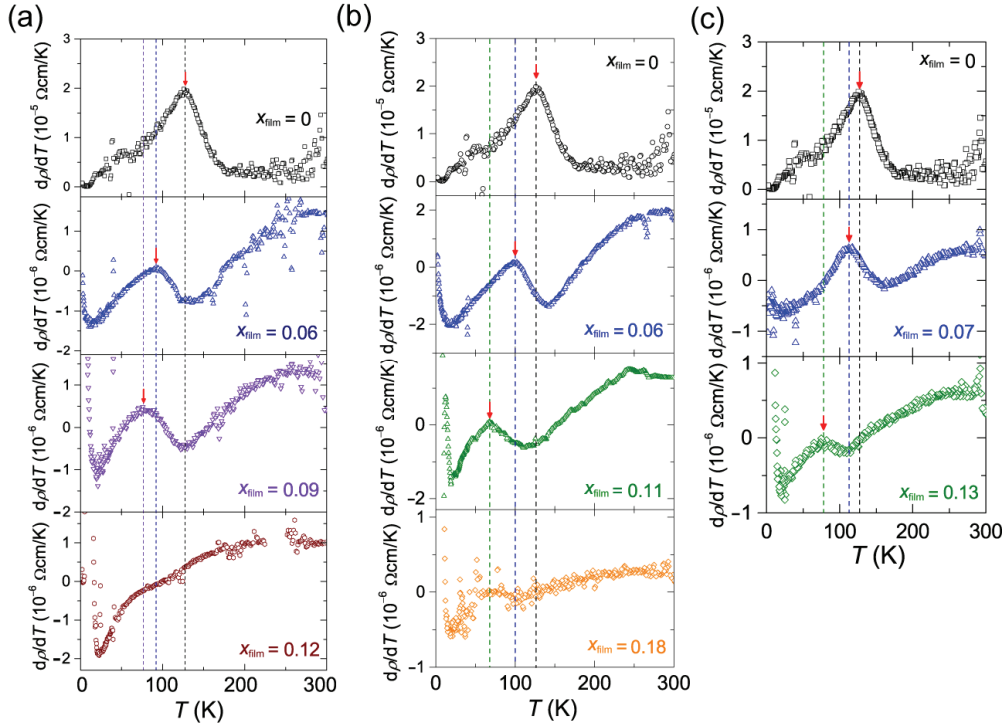


Figure S3 $d\rho/dT$ curves of (a) $(\text{Ba}_{1-x}\text{Ce}_x)\text{Fe}_2\text{As}_2$ with $x_{\text{film}} = 0-0.12$, (b) $(\text{Ba}_{1-x}\text{Pr}_x)\text{Fe}_2\text{As}_2$ with $x_{\text{film}} = 0-0.18$, and (c) $(\text{Ba}_{1-x}\text{Nd}_x)\text{Fe}_2\text{As}_2$ with $x_{\text{film}} = 0-0.13$. The doping concentration x_{film} is indicated on right-bottom of each figure. The positions of T_{anom} are indicated by the red vertical arrows.

IV. Field dependence of magnetoresistance

Figure S4 shows the magnetoresistance (MR) of $(\text{Ba}_{0.72}\text{Ce}_{0.28})\text{Fe}_2\text{As}_2$ epitaxial film measured at (a) 30K, (b) 10 K, and (c) 2 K. The MR were measured under magnetic field parallel to the c -axis and the ab -plane, respectively. With decreasing the temperature, the negative MR steeply increases and the transition magnetic field from the $-\alpha H^2$ dependence to the $-\alpha \log H$ dependence shifts to a lower H . In addition, the negative MR with $H//ab$ is much smaller than that with $H//c$ for all the temperatures. This result indicates that the spin ordering of Ce should be antiferromagnetic parallel to the c -axis and ferromagnetic parallel to the ab -plane.

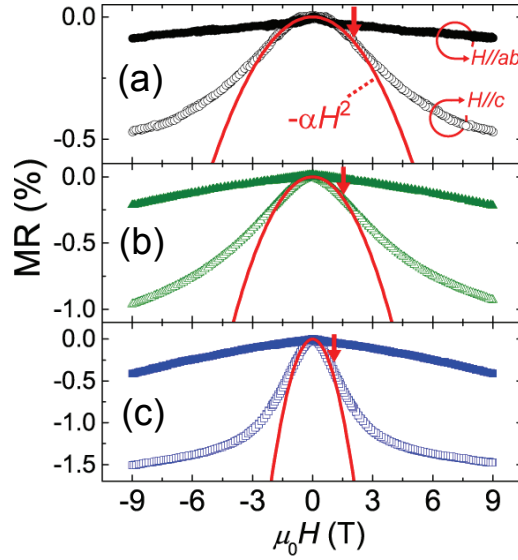


Figure S4 $MR = [\rho(\mu_0 H) - \rho(0)] / \rho(0) \times 100$ measured at (a) 30 K, (b) 10 K, and (c) 2 K for $(Ba_{0.72}Ce_{0.28})Fe_2As_2$ epitaxial film. Open and closed symbols indicate MR under fields (H) parallel to c -axis and to the ab -plane, respectively. The electric current for MR was applied along the ab -plane and perpendicular to both of the magnetic field directions. The solid red lines represent the fitting results with the $-\alpha H^2$ behavior. The red vertical arrows indicate the transition magnetic fields from the $-\alpha H^2$ dependence to the $-\alpha \log H$ dependence.

Reference

[S1] Katase T, Hiramatsu H, Kamiya T and Hosono H 2010 *Appl. Phys. Express* **3** 063101